Electronic Mode Stirring for Improved Backscatter Communication Link Margin in a Reverberant Cavity Animal Cage Environment

James D. Rosenthal, *Student Member, IEEE,* Alexandra Pike, Sara Reyes, *Student Member, IEEE,* and Matthew S. Reynolds, *Senior Member, IEEE*

***Abstract*—Neuroscience research in non-human primates (NHPs) often requires multi-day neural recordings from freely moving animals inside their home cages, making ultra-low power uplinks using wireless backscatter communication highly desirable. Previous work reveals that the channel transfer function (CTF) of a standard NHP home cage in the 915 MHz and 2.4 GHz industrial, scientific, and medical (ISM) bands resembles a resonant cavity exhibiting deep nulls throughout the cage volume, which are particularly acute for round-trip backscatter paths.**

In this work, we investigate a novel application of passive antenna mode stirring via switched parasitic antennas (SPAs) to reduce the magnitude and prevalence of deep nulls in the cage CTF. We present a system leveraging four cage-ceiling-mounted SPAs with two dynamically-controlled impedance states each, yielding 16 total mode stirring configurations. We compare frequency domain power ratio measurements at 126 positions throughout the cage taken with and without passive antenna mode stirring. In the 915 MHz ISM band, the optimized SPA configuration improved the maximum two-way insertion loss in 68% of testing locations, reducing the worst-case two-way insertion loss by 60.2 dB. In the 2.4 GHz ISM band, the maximum two-way insertion loss was improved in 53% of testing locations, reducing the worst-case two-way insertion loss by 35.6 dB. This approach eliminates the deepest nulls in the cage volume and leads to significantly improved link margin for a backscatter-based wireless brain computer interface (BCI).

***Index Terms*—Backscatter communication, full-duplex radios, intelligent reflective surfaces, neural recording, reverberant cavity**

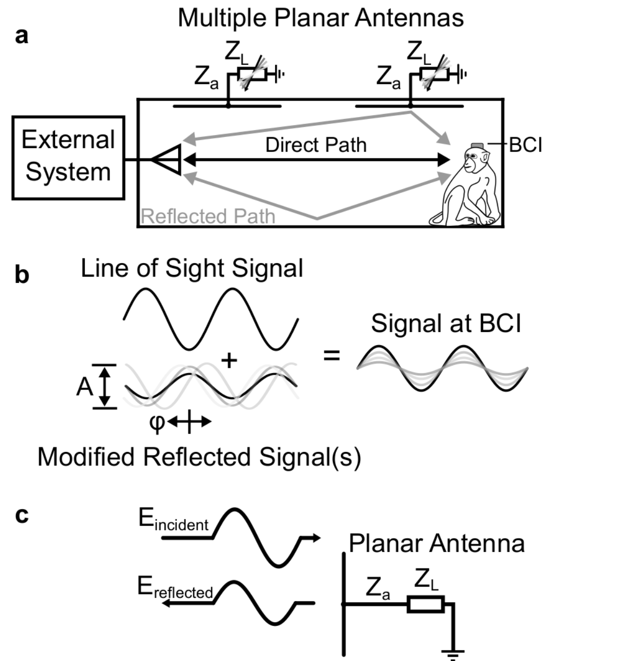

Fig. 1. (a) Overview of the proposed passive antenna mode stirring technique, (b) Multipath produces destructive interference in certain locations throughout the animal cage. (c) passive antenna mode stirring dynamically alters the amplitude and phase of reflection by controlling the impedance presented to a planar antenna.

I. INTRODUCTION

ELECTROPHYSIOLOGICAL recording in non-human primates (NHPs) seeks to understand how low-level neural activity gives rise to higher levels of behavior [1]. While significant findings continue to be made from head-fixed experiments in controlled environments, there has been growing demand in the neuroscience research community for wireless brain-computer interfaces (BCIs) that can stream neural recordings from freely moving animals over long durations (>2 days) [2], [3]. These wireless experiments could yield new insights into long-term neural dynamics involved in healthy and pathological states while reducing unnatural correlations in data and alleviating the stress of physical restraints on the animals [4] .

Power-hungry wireless data uplinks remain an obstacle in the pursuit of long duration neural recording from freely moving animals. The size and weight of batteries in BCIs must be minimized to avoid impeding movement or injuring the animals. With typical BCI battery size constraints of 1-3 cm^3, the device battery is depleted within hours. The short battery life results from the 10-100 mW transmitter power consumption of standard wireless approaches such as Wi-Fi (e.g. IEEE 802.11n) and Bluetooth Low Energy [5], [6]. To reduce the energy burden of wireless telemetry, backscatter communication is being explored for BCIs due to its small form-factor, high data rates, and orders-of-magnitude lower power consumption relative to standard wireless systems [7]–

Manuscript received Mon. Day, 2021; revised Mon. Day, 2021; accepted Mon. Day, 2021. Date of publication Mon. Day, 2021.

Corresponding authors: J. Rosenthal (e-mail: jamesdrosenthal@gmail.com) and M.S. Reynolds (e-mail: matt.reynolds@ece.uw.edu)

J.D. Rosenthal, S. Reyes, and M.S. Reynolds are with the Department of Electrical & Computer Engineering, University of Washington, Seattle, WA 98195, USA.

A. Pike is with Juanita High School, Kirkland, WA, USA.

This material is based upon work supported by the National Science Foundation Graduate Research Fellowship under Grant No. DGE-1762114 and in part by Award Number EEC-1028725 from the National Science Foundation.

Color versions of one or more of the figures in this letter are available online at http://ieeexplore.ieee.org.

Digital Object Identifier 10.1109/TMTT.2021.0000000

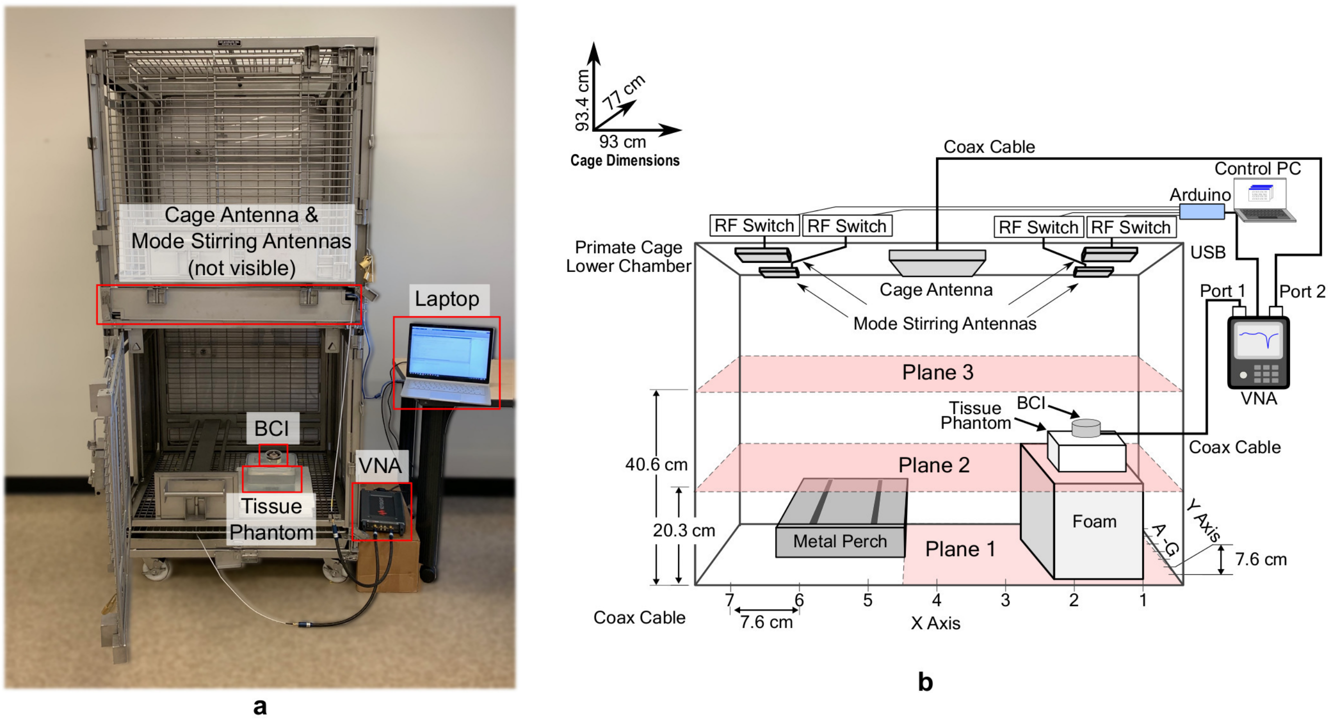

Fig. 2. (a) Photo and (b) Block diagram of the test setup used to characterize the 915 MHz and 2.4 GHz ISM-band wireless channel inside the NHP cage using passive antenna mode stirring.

[10]. Backscatter communication achieves high per-bit energy efficiencies by removing the power hungry functions of RF carrier generation and RF amplification from the BCI. Data is transmitted via load modulation, where the impedance presented to the BCI antenna is deliberately changed to reflect an externally-generated carrier.

The improved energy efficiency of backscatter communication comes at the cost of a less favorable link budget compared to conventional radios. Because the externally-generated carrier wave travels a round trip from the external system to the backscatter radio and back, the RF power at the receiver changes as $1/r^4$ for a backscatter system, rather than the usual $1/r^2$ for conventional radios, where r is the free-space distance between the external system and the BCI antenna [11], [12]. Given the round-trip nature of the backscatter link budget, multipath inside the cage can significantly reduce the reliability of backscatter radios. Previous characterizations of the 915 MHz and 2.4 GHz ISM bands within NHP cages indicate that the metal walls form a reverberant cavity that exhibits deep nulls throughout the cage volume [13], [14]. These findings suggest that additional measures are needed to alleviate deep nulls in the channel transfer function (CTF).

Two main approaches have been explored to reduce or overcome multipath interference in a cage. In [15], a custom RF-transparent NHP cage was built and validated with simulations, measurements, and *in vivo* wireless measurements. Reducing the conductivity of the cage structure significantly improved wireless system performance, however, most RF-transparent materials are both much more expensive and less rugged than conventional metal cages. To avoid the spread of disease in animal care facilities, the animal cages must be frequently autoclaved and/or cleaned with reactive chemicals like bleach, both of which rapidly degrade RF-transparent plastics.

Other research has explored how antenna diversity at the external system and/or backscatter radio (e.g. in a MIMO system) can mitigate the effects of nulls [3], [16]–[19]. These schemes depend on multiple antennas separated by one or more wavelengths to provide spatial diversity. However, diversity and MIMO approaches are often not suitable for biomedical applications where the device dimensions (typically 1-3 cm^3) are physically small relative to the operating wavelength of the wireless system. For small implantable devices in particular, the device size is so small that, even if multiple antennas were implemented, they would exhibit very high mutual coupling which would negate any advantage from a MIMO approach.

In this work, we present a different approach for mitigating multipath fading in a metal NHP cage via mode stirring. By altering the electromagnetic boundary conditions of the cage, nulls in the CTF can be reduced and a more favorable link budget achieved (Fig. 1(a)). Mode stirring is used to improve the statistical uniformity of the electric field within reverberant cavities for electromagnetic interference and compatibility (EMI/EMC) testing [20], [21]. It can be achieved via mechanical and electronic means, though mechanical mode stirring would be impractical for in-cage animal experiments because a reflector must be mechanically displaced, potentially interfering with the NHP. In contrast, passive antenna mode stirring using low profile antennas could enable control of the CTF without requiring intrusive structures. passive antenna mode stirring has shown promising results for EMI/EMC applications, e.g. in [22], where reactively-loaded conical antennas were placed around the cavity to improve the field isotropy and homogeneity. The loads presented to the antennas were changed to modify the amplitude, A, and phase, ϕ, of the reflected electric field (Fig. 1(b)). Similar approaches have seen success using switched parasitic antennas (SPAs) for beamforming to improve the received signal strength of sensor nodes using backscatter communication [23]–[26] and tunable metasurface reflect arrays to electronically modify the boundary conditions of a reverberant cavity [27]. To the best of our knowledge though, this work is the first to propose using low-profile SPAs to implement passive antenna mode stirring inside the animal cage.

Our experimental results demonstrate that passive antenna mode stirring using SPAs can significantly reduce the worst-case insertion loss within a cage. We present comparisons of the CTF within a NHP cage taken with and without mode stirring in the 915 MHz and 2.4 GHz ISM bands. These findings represent a unique contribution to the field of applied electromagnetics:

- **Suitability for biomedical device applications:** The passive antenna mode stirring approach imparts no additional hardware or software complexity on the size- and energy- constrained biomedical device, and it can be implemented in standard metal animal cages. Unlike MIMO methods requiring multiple antennas with minimal mutual coupling, which is difficult to implement on a size constrained device, the mode stirring approach can leverage a single antenna on the biomedical device. Future iterations could be tractably adapted for more complex applications, including closed-loop CTF control to adapt the mode stirring configuration to the movement of the animal within the cage.
- **Platform Flexibility:** The benefits of the passive antenna mode stirring architecture could enable higher data rates and lower power consumption for both backscatter and conventional radios. The results from this paper can be generalized to other arenas of varying size and geometry.
- **Dynamic Control:** The passive antenna mode stirring configurations can be controlled quickly (nanoseconds) without obtrusive mechanical assemblies, enabling the mode stirring configuration to be changed as the NHP moves inside the cage. Dynamic control opens the door for future interdisciplinary work integrating communication theory, control theory, and experimental neuroscience.

In this paper, Section II presents a description of the experimental setup, the NeuroDisc BCI and the mode stirring architecture. Section III presents the experimental methods, results, and a discussion of the findings. Lastly, Section V provides conclusions and ideas for future research.

II. Channel Transfer Function Measurements

A. Experimental Environment

Metal Non-Human Primate (NHP) Cage

Measurements were conducted in the lower chamber of a standard double-height NHP cage provided by the Washington National Primate Research Center (Fig. 2). This work was conducted with tissue phantoms instead of live animals, so no animal use authorization was required. The lower chamber has external dimensions of 93.4 cm × 93 cm × 77 cm (height × width × length). All six cage sides are made of a metal mesh with a mean grid spacing of 2.5 cm. The ceiling of the lower chamber is additionally under the solid metal bed pan of the upper chamber. A 60.7 cm × 23.4 cm polycarbonate window is inset into one cage wall, and inside the cage there is an 18 cm × 15 cm metal perch for the NHP which is welded in place and cannot be moved. The mean grid spacing of the mesh is more than 10× smaller than the shortest wavelength of the 915 MHz ISM band ($\lambda \approx 32.3$ cm) and 6× smaller than the shortest wavelength of the 2.4 GHz ISM band ($\lambda \approx 12$ cm).

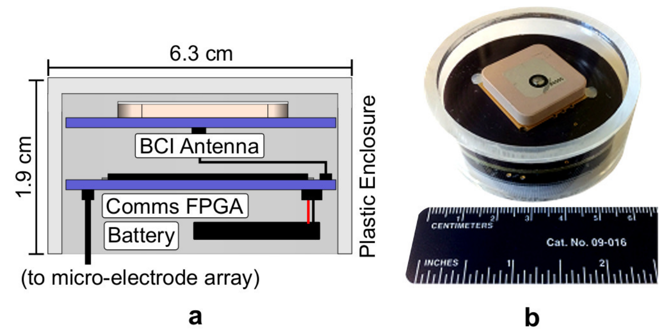

Fig. 3. (a) Drawing and (b) Photo of the NeuroDisc BCI.

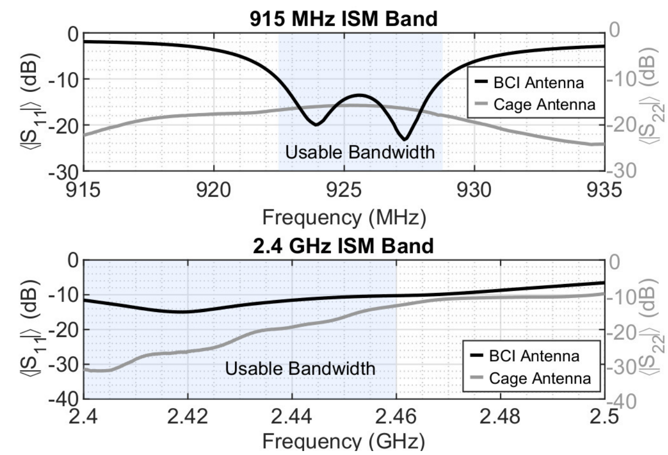

Fig. 4. Measured ensemble average return loss of the BCI antenna, $\langle S_{11} \rangle$, and the cage antenna, $\langle S_{22} \rangle$ without mode stirring antennas for the (top) 915 MHz ISM band and (bottom) 2.4 GHz ISM band. The usable bandwidth (shaded region) was determined by the BCI antenna's performance.

A total of 126 measurements were made at locations across three measurement planes: 28 locations on Plane 1, 49 locations on Plane 2, and 49 locations on Plane 3. The vertical spacing between measurement planes was 20.3 cm. Each measurement plane was subdivided into a grid with 7.6 cm spacing, with the X axis labelled *A* through *G* and the Y axis labelled *1* through *7*. Measurements were conducted in the center of the grid squares, as shown in Fig. 2(b). RF-transparent foam blocks were used to elevate the tissue phantom for Planes 2 and 3, and the foam was removed for measurements in Plane 1. Columns 5-7 on the bottom measurement plane (Plane 1) were inaccessible due to the metal perch, which cannot be removed. In this index scheme, position D4 corresponds to the center of the cage.

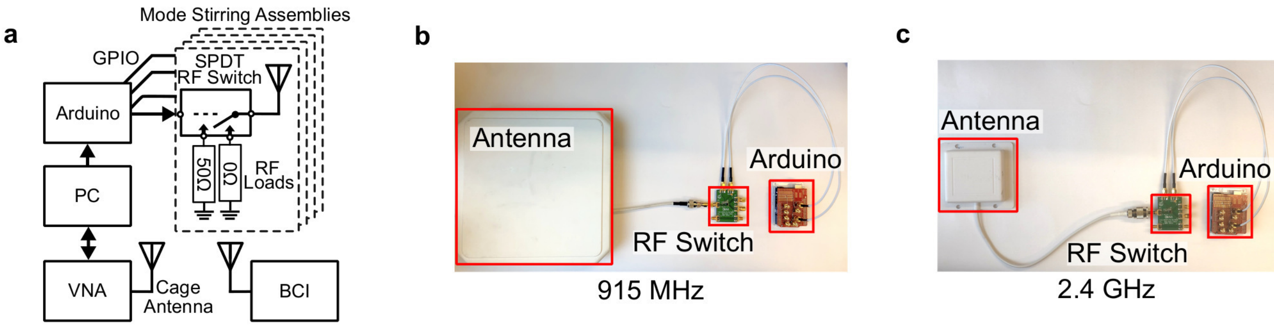

Fig. 5. Block diagram (a) and photos of a single mode stirring assembly used for 915 MHz (b) and 2.4 GHz (c).

B. Experimental Equipment

Vector Network Analyzer

S-parameter measurements were made using a two-port Keysight P9375A Vector Network Analyzer (VNA) controlled by a laptop (Fig. 2). Prior to the measurements, a two-port VNA calibration was performed to set the measurement reference plane at the BCI and external antenna ports, calibrating out the phase shift and attenuation of the cables. At each measurement point, the cables were dressed to the cage walls to minimize their influence on the measurements.

Tissue Phantom

A tissue phantom that approximates the dielectric effects of a typical juvenile male rhesus macaque was used for all measurements. The tissue phantom consists of a 19.5 cm × 12.0 cm × 11.0 cm plastic container filled with 2.5 liters of tissue-equivalent saline solution (0.91 g NaCl per liter of distilled water).

NeuroDisc Brain-Computer Interface (BCI)

The NeuroDisc BCI was used for measurements in both the 915 MHz and 2.4 GHz ISM bands. A graphical depiction of the NeuroDisc is shown in Fig. 3(a) and a photo is shown in (b) with the 2.4 GHz antenna. The NeuroDisc consists of an antenna, a Communication (Comms) FPGA board incorporating the backscatter modulator, and a battery within a plastic housing (Fig. 3) [9], [10].

The NeuroDisc was configured for each frequency band by connecting the appropriate BCI antenna. A semi-custom antenna was used, made from an off-the-shelf ceramic antenna element and a custom PCB. The same PCB was used for both frequency bands, and it consisted of a circular, 5.5 cm diameter, two-layer FR-4 PCB with 1.6 mm dielectric thickness and 30 μm copper trace thickness. The top side of the BCI antenna PCB contained a centered, circularly shaped ground plane and a ceramic patch antenna. For the 915 MHz band, an Abracon APAE915R2540ABDB1-T antenna with dimensions 2.5 cm × 2.5 cm × 0.4 cm is used; for the 2.4 GHz band, a Tagolas Inc. WLP.2450 antenna with dimensions 2.5 cm × 2.5 cm × 0.4 cm is used. The bottom of the PCB had a UMCC coaxial connector, allowing the antenna to connect to the Comms FPGA board via a 5 cm UMCC-to-UMCC coaxial cable. Previous simulations of the 915 MHz ceramic antenna mounted to antenna PCB found a realized gain of -0.4 dBi at 923 MHz [13]. Given the similarities between the 915 MHz and 2.4 GHz ceramic antenna elements, similar gain performance should be expected.

The average measured reflection coefficients of the BCI antennas and the cage antenna are plotted in Fig. 4 for the 915 MHz (top) and 2.4 GHz (bottom) bands. The BCI antenna was connected to port 1 of the VNA with a coaxial cable and placed on top of a tissue phantom inside the cage; the cage antenna was connected to port 2 of the VNA. The measurements in Fig. 4 show the average S_{11} (for the BCI antenna) and S_{22} (for the cage antenna) across all positions in the cage. To determine the usable bandwidth of each BCI antenna on each frequency band, the ensemble average of S_i was taken across all positions,

$$\langle|S_i(f)|\rangle = \frac{1}{N}\sum_{k=1}^{N}|S_i^{(k)}(f)| \tag{1}$$

where N is the total number of measurement positions in the cage and $|S_i^{(k)}(f)|$ is the magnitude of the measured reflection coefficient at position k across the entire frequency band for port i of the VNA. For $N = 126$ and measuring at 1000 frequency points from 850-950 MHz and 2.400-2.500 GHz, the usable 10 dB impedance bandwidth was found to be 922.5-928.8 MHz (6.3 MHz) for the 915 MHz ISM band and 2.4000-2.4648 GHz (64.8 MHz) for the 2.4 GHz ISM band (Fig. 4).

Cage Antenna

A cage antenna representing a monostatic backscatter communication antenna [12] was affixed on the inside of the mesh wall separating the upper and lower chambers of the NHP cage, as shown in Fig. 2(b). For measurements in the 915 MHz band, we used a Laird Technologies S9028PCR 9 dBi right-hand circularly polarized (RHCP), air dielectric patch antenna with a 3 dB-beamwidth of 70 degrees azimuth. For measurements in the 2.4 GHz band, we used an L-Com Inc. 2.4 GHz 8 dBi RHCP antenna with a 3 dB-beamwidth of 65 degrees azimuth. The average measured reflection coefficient of the antenna for each frequency band is plotted in Fig. 4.

Mode Stirring Assemblies

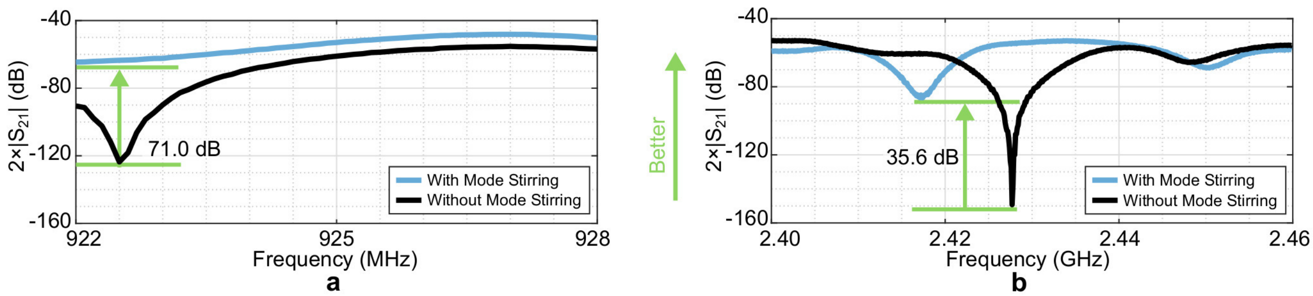

Fig. 6. Plots comparing the worst-case insertion loss $|S_{21}|$ across all positions with and without passive antenna mode stirring for (a) the 915 MHz ISM band at plane 1, row 2, column G (best mode stirring configuration: 16); and (b) 2.4 GHz ISM band at plane 1, row 3, column C (best mode stirring configuration: 16).

For the mode stirring measurements in each frequency band, we installed a band-specific mode stirring assembly into the NHP cage. The assembly was comprised of several components (Fig. 5): four mode stirring antennas selected for the particular frequency band; four Analog Devices ADG918 single-pole dual throw (SPDT) RF switch evaluation boards (one for each mode stirring antenna) with 50Ω and short circuit terminations; and one Arduino UNO with a daughter board for routing 3.3V power and digital control signals to the RF switches. A PC controlled the Arduino UNO using MATLAB (MathWorks) to digitally actuate the four RF switches. With four mode-stirring antennas each having two possible impedance states, 16 total mode stirring configurations were possible (e.g. all four shorted, three shorted and one with a 50Ω load, etc). For the 915 MHz band measurements, we used L-Com HG8909P linearly polarized antennas with 9 dBi of gain and a 3 dB-beamwidth of 70 degrees in the horizontal plane and 60 degrees in the vertical plane. For the 2.4 GHz band measurements, we used L-Com HG2408P linearly polarized antennas with 8 dBi of gain and a 3 dB-beamwidth 75 degrees in the horizontal plane and 65 degrees in the vertical plane. Note that the mode stirring assemblies were entirely removed from the cage for the measurements designated as *without mode stirring*.

III. Experimental Methods & Results

A. Measuring the Channel Transfer Function

For each ISM frequency band, two sets of measurements were taken: one set *without* mode stirring (baseline) and one set *with* mode stirring (experimental). The mode stirring assemblies were not installed in the cage during the baseline measurements. The baseline measurements are technically a form of position stirring due to the changing position of the tissue phantom and BCI antenna within the cage. In practice, this form of position stirring would be randomly executed by the monkey. To clearly distinguish the deliberate mode stirring of our system from this random mode stirring by the monkey, the baseline measurements are denoted as *without mode stirring*.

After completing the baseline measurements, the cage antenna was left in the same position, and the mode stirring assemblies were installed. Each mode stirring antenna was mounted in a corner of the steel mesh ceiling with the same orientation with respect to the antennas' polarization. The mode stirring antennas were connected to the RF switches and Arduino, which all sat outside of the testing volume to minimize interference. A graphical depiction of the test setup is shown in Fig. 2.

The measurements were conducted by first positioning the BCI and tissue phantom at the center of the desired position in the cage. For the baseline measurements, the two-port S-parameters were measured using the VNA. At each measurement position, a MATLAB script was used to sequentially change the mode stirring configuration and measure the two-port S-parameters until all 16 mode stirring configurations had been measured. The BCI and tissue phantom were then moved to the next position, and the process was repeated until baseline and experimental measurements were made at all 126 positions in the cage. The BCI antenna orientation was maintained constant at each measurement points, and the cables were dressed to the cage walls at each position to minimize their influence on the measurements. Measurements for both frequency bands were taken using 100 kHz steps in the frequency domain.

B. Characterizing the Channel Transfer Function

Knowledge of the insertion loss throughout the cage provides insight into the link margin and reliability of communication systems. For a backscatter communication system assuming negligible impedance mismatches at the antennas, the link margin can be calculated as

$$P_R = P_{\text{CW}} - IL_{\text{two-way}} + M - L_{\text{sys}} \tag{2}$$

where P_R is the received power at the cage antenna in dBm, P_{CW} is the power of the RF carrier wave presented to the cage antenna in dBm, IL is the insertion loss in dB, M is the modulation factor corresponding to the amount of power backscattered from the modulator, and L_{sys} represents additional system losses in the full-duplex monostatic backscatter receiver [12], [13]. The worst-case insertion loss at a position in the cage will determine the backscatter link margin and the uplink reliability for a given receiver sensitivity and system parameters in Eq. 2.

The CTF of the cage was thus characterized using frequency domain power ratio measurements to determine the insertion loss at each position. With the VNA, the transmission coefficient S_{21} was measured at each position in 100 kHz steps over the BCI antenna's average -10 dB bandwidth (Sec. II-B), then converted to two-way insertion loss in decibels

$$IL_{\text{two-way}}(f,k) = 2 \times \big(-20 \times \log_{10}(|S_{21}(f,k)|)\big) \tag{3}$$

where f is frequency and k is the measurement position. The factor of two accounts for the round-trip path of the carrier wave from the cage antenna to the BCI antenna and back. For brevity, we refer to $IL_{\text{two-way}}$ as IL for the remaining equations.

To determine how passive antenna mode stirring affected the cage CTF, we compared the worst-case insertion loss at each position without mode stirring, to the worst-case insertion loss from the mode stirring configuration having the lowest insertion loss. In the baseline case without mode stirring, the worst-case insertion loss corresponded to the maximum insertion loss value across all frequency points:

$$IL_{\text{worst-case}} = \max(IL). \tag{4}$$

In the experimental case using mode stirring, the worst-case insertion loss was a function of the mode stirring configuration, indexed by i. We first calculated the worst-case insertion loss for each mode stirring configuration at a specific point, resulting in a 16 element vector, $IL_{\text{worst-case}}(i)$. The argument that minimized the vector corresponded to the best mode stirring configuration for that position:

$$\text{Best Config.} = \arg\min(IL_{\text{worst-case}}(i)). \tag{5}$$

Plots of the worst-case measured insertion loss $|S_{21}|$ for the 915 MHz and 2.4 GHz bands are shown in Fig. 6(a) and (b), respectively. These plots show how mode stirring improves the worst-case insertion loss for a single point in each frequency band.

To compare the worst-case insertion loss across all BCI positions for the baseline and experimental measurements, heatmaps of the measurements were compiled showing the results for the 915 MHz band in Fig. 7 and for the 2.4 GHz band in Fig. 8. In these figures, lighter colors represent a lower insertion loss, and thus more favorable channel loss characteristics. Histograms of the worst-case insertion loss for both frequency bands are shown in Fig. 9.

Additional statistics were calculated and compiled in Table I for the 915 MHz band and in Table II for the 2.4 GHz band. The mean two-way IL (dB) across a plane, $\overline{IL}(p)$, was calculated as

$$\overline{IL}(p) = \sum_{x,y} \frac{\overline{IL}(p,x,y)}{n(x)n(y)} \tag{6}$$

where $n(\cdot)$ represents the number of elements in the set, p represents the measurement plane, x represents the column, y represents the row, and $\overline{IL}(p,x,y)$ is the mean two-way IL at a specific position

$$\overline{IL}(p,x,y) = \sum_{f} \frac{IL(f,p,x,y)}{n(f)}. \tag{7}$$

The average standard deviation of the insertion loss, $\bar{\sigma}(p)$, for each plane was calculated as

$$\bar{\sigma}(p) = \sum_{x,y} \frac{\sigma(p,x,y)}{n(x)n(y)} \tag{8}$$

where

$$\sigma(p,x,y) = \sqrt{\frac{\sum_f \left|IL(f,p,x,y) - \overline{IL}(p,x,y)\right|}{n(f)-1}}. \tag{9}$$

IV. Results & Discussion

The statistics in Table I and Table II demonstrate that mode stirring reduced the overall severity and prevalence of deep nulls in the cage CTF. Interestingly, mode stirring does not improve insertion loss at every position or at every frequency. For example, in Fig. 6(b) the insertion loss with mode stirring is worse than without mode stirring between 2.41-2.42 GHz approximately. In a minority of positions, an increase in the worst-case insertion loss at certain points can be observed in the heatmaps, for example at position A1 of Measurement Plane 1 in the 2.4 GHz ISM band.

A. Mode Stirring Reduced Worst-Case Insertion Loss at Most (but not all) Positions

Measurements indicate that mode stirring reduced the worst-case insertion loss for most positions in both frequency bands. In the 915 MHz ISM band across all 126 measurement positions, 86 (68.25%) exhibited a reduction of the worst-case insertion loss when mode stirring was used. The worst-case insertion loss across the entire cage improved by 30.10 dB, while the mean insertion loss improved by 3.68 dB across Plane 1, improved by 0.87 dB across Plane 2, and worsened by 1.37 dB across Plane 3. Of the 86 positions that showed an improvement in worst-case insertion loss, 60 positions (47.62% of all positions) had a reduction >6 dB. The average standard deviation of the insertion loss between measurement locations was reduced between 0.29-1.23 dB across all planes, indicating increased uniformity in the insertion loss.

In the 2.4 GHz ISM band across all 126 measurement positions, 67 (53.17%) exhibited a reduction of the worst-case insertion loss when mode stirring was used. The worst-case insertion loss across the entire cage decreased by 17.81 dB. The mean insertion loss increased by 0.41 dB across Plane 1 and by 0.58 dB across Plane 2; across Plane 3 it decreased by 0.35 dB. Of the 67 positions that showed a reduction in worst-case insertion loss, 51 positions (40.48% of all positions) had a reduction >6 dB. The average standard deviation of the insertion loss between measurement locations showed minor changes, reducing between 0.14-0.26 dB across Planes 1 and 2, and increasing by 0.07 dB across Plane 3.

At isolated positions in both frequency bands, mode stirring appears to have increased the worst-case insertion loss relative to the baseline measurements. In the 915 MHz ISM band, the worst-case insertion loss worsened at 40 positions (31.75%) with mode stirring. Of those positions, 26 (20.63% of all

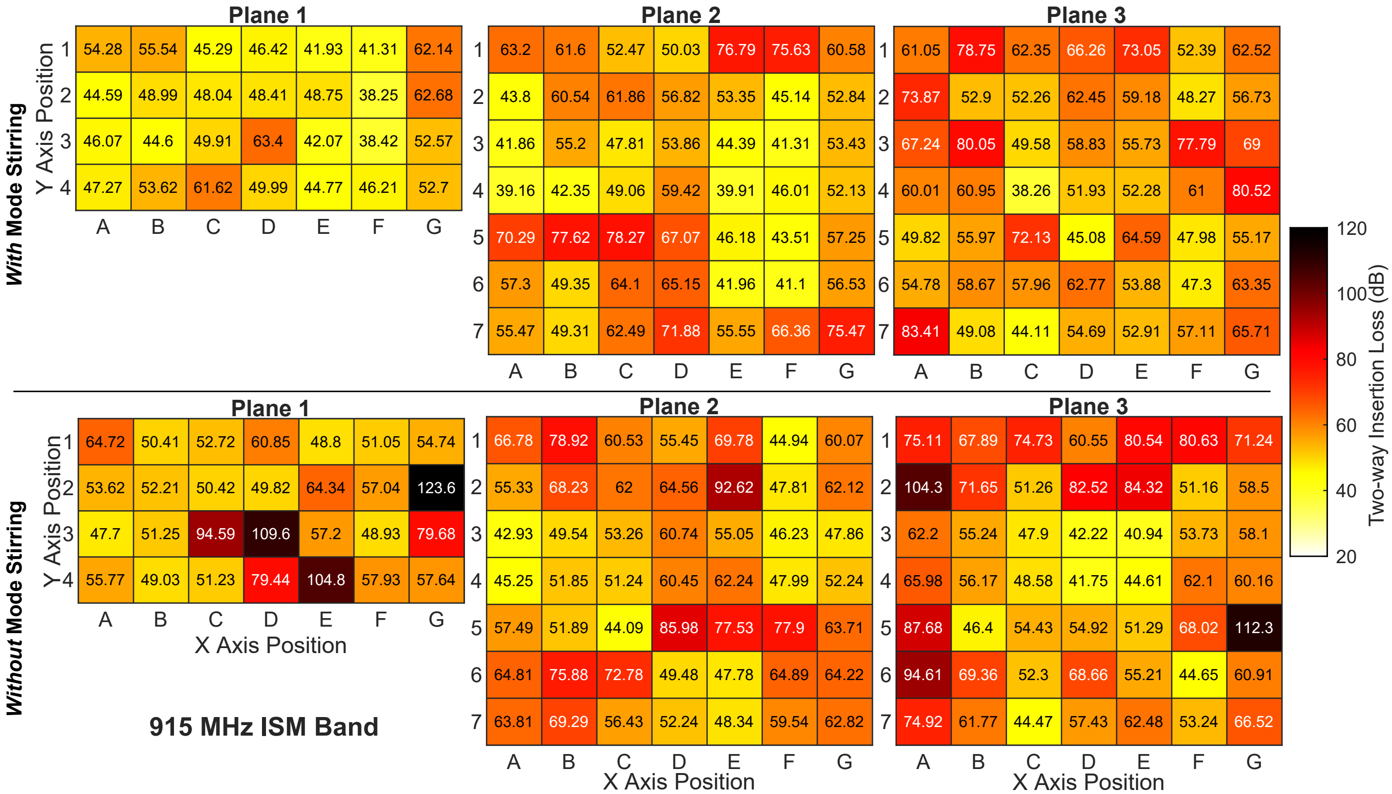

Fig. 7. Experimental results for the 915 MHz ISM band comparing the highest two-way insertion loss at each measurement point. In all heatmaps, lighter colors indicate lower insertion loss and thus better performance.

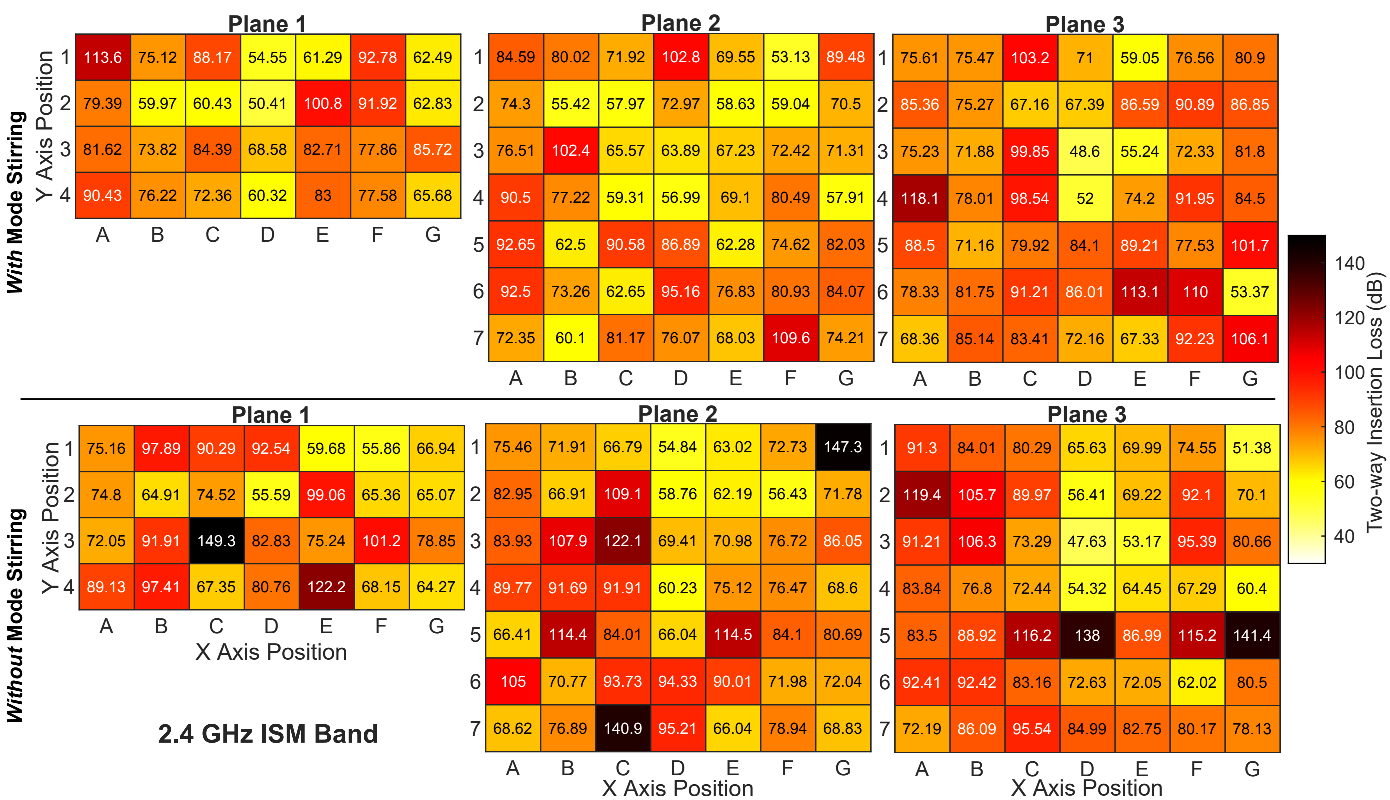

Fig. 8. Experimental results for the 2.4 GHz ISM band comparing the highest two-way insertion loss at each measurement point. In all heatmaps, lighter colors indicate lower insertion loss and thus better performance.

TABLE I
915 MHz Two-Way Channel Transfer Function Measurement Summary

	Plane 1			Plane 2			Plane 3		
	Without MS	With MS	Change	Without MS	With MS	Change	Without MS	With MS	Change
Mean IL (dB)	50.74	43.38	-7.36	50.26	48.52	-1.74	50.54	53.28	+2.74
Worst-Case IL (dB)	123.6	63.4	-60.20	92.62	78.28	-14.34	112.28	83.42	-28.86
IL Std. Dev. (dB)	5.18	2.72	-2.46	4.34	3.76	-0.58	5.18	4.42	-0.76

TABLE II
2.4 GHz Channel Transfer Function Measurement Summary

	Plane 1			Plane 2			Plane 3		
	Without MS	With MS	Change	Without MS	With MS	Change	Without MS	With MS	Change
Mean IL (dB)	56.88	57.70	+0.82	58.30	59.46	+1.16	59.82	59.12	-0.70
Worst-Case IL (dB)	149.26	113.64	-35.62	147.30	109.58	-37.72	141.38	118.12	-23.26
IL Std. Dev. (dB)	7.78	7.50	-0.28	7.84	7.32	-0.52	8.22	8.36	+0.14

positions) showed an increase of more than 6 dB. The largest increase in worst-case insertion loss was by 34.2 dB.

In the 2.4 GHz ISM band, the worst-case insertion loss worsened at 59 positions (46.83%) with mode stirring enable. Of those positions, 35 (27.78% of all positions) showed an increase of more than 6 dB. The largest increase in the worst-case insertion loss was 48.02 dB.

B. Limitations of the Mode Stirring Implementation

The measurements using mode stirring demonstrated an observable reduction of the worst-case insertion loss within the cage across a majority of positions. The heatmaps in Fig. 7 and Fig. 8 show that, overall, the magnitude of deep nulls in the CTF decrease when passive antenna mode stirring is used. These observations are supported by the statistics in Table I and Table II, where we observed that the worst-case mean two-way insertion loss was reduced by more than 7 dB in the 915 MHz ISM band and by more than 11.63 dB in the 2.4 GHz band. These changes to the CTF in both frequency bands can be seen in the histograms of Fig. 9. We observed that the grouping of worst-case two-way insertion loss counts is shifted to lower values when mode stirring is introduced, and that the high insertion loss values from measurements without mode stirring disappear.

The heatmaps in Fig. 7 and 8 reveal that mode stirring increased the insertion loss at some positions relative to the baseline measurements. It is possible that the passive antenna mode stirring system contributes to additional destructive interference to the line-of-sight path that cannot be overcome by changing the system's terminating impedances. The passive antenna mode stirring system in this work used a 50 Ω load and a short-circuit load. These terminations may be inadequate for reflecting energy with the correct phase and amplitude to improve the CTF at every position in the cage. Since the 50 Ω load absorbs energy from the cage, it would be interesting to repeat measurements using an open-circuit load instead. Other possible causes for the increased insertion loss are the polarization and placement polarization of the mode stirring assembly antennas. The mode stirring assemblies used antennas with linear polarization, which may have increased the sensitivity of the insertion loss measurements to the BCI orientation. Furthermore, the symmetric spacing of mode stirring assemblies on the cage ceiling may not be optimal, considering the asymmetric construction of the cage with the metal perch and the polycarbonate window.

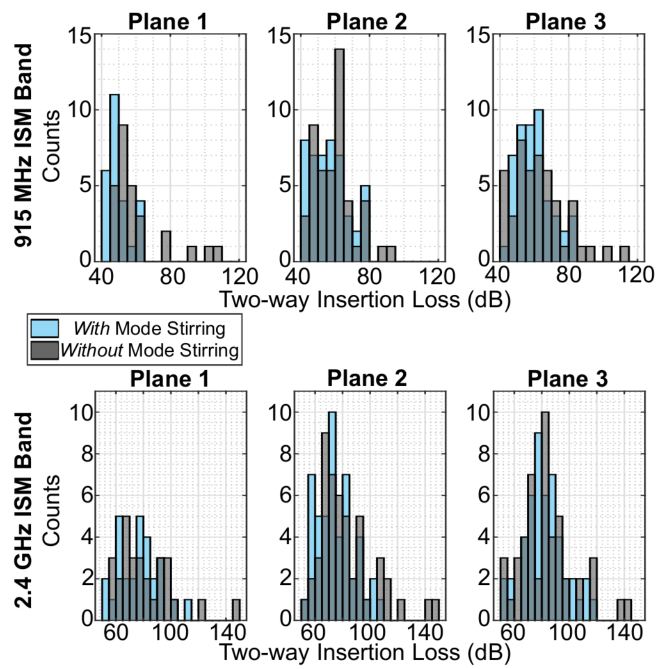

Fig. 9. Histogram of highest insertion loss for each measurement point in the 915 MHz ISM band (top) and 2.4 GHz ISM band (bottom), comparing results with and without passive antenna mode stirring.

In both frequency bands and in both configurations (with and without mode stirring), insertion loss was higher at measurement plane 3. We believe this increase in insertion loss may be due to degraded line of sight between the BCI antenna and the cage antenna and possibly near-field interactions between the two antennas.

Overall, the improved insertion loss statistics throughout the cage suggests that passive antenna mode stirring has the potential to increase the channel capacity of the NHP cage and bolster the reliability and/or data rates of wireless communication systems in the cage.

V. Conclusions & Future Work

In this work, we explored a novel implementation of passive antenna mode stirring in a non-human primate (NHP) cage. Using switched parasitic antennas (SPAs) mounted to the ceiling of the cage and measuring the power ratio between a BCI antenna and a ceiling-mounted cage antenna, we found that passive antenna mode stirring can create a more favorable communication channel in both the 915 MHz and 2.4 GHz ISM bands. We specifically observed that the use of SPAs improved the worst-case insertion loss by up to 60.20 dB in the 915 MHz band and by up to 35.62 dB in the 2.4 GHz band. These reductions in insertion loss increase the channel link margin and thus the overall channel capacity for wireless uplinks.

The results suggest that passive antenna mode stirring is a promising technique to improve the performance of ultra-low power backscatter wireless uplinks for BCIs. Further work is required to continuously optimize the mode stirring configuration given changes in the cage environment as the NHP moves throughout the cage. To implement real-time mode stirring optimization, a closed-loop optimization approach could be implemented where the mode stirring configuration is selectively changed to maximize the received backscatter signal power as the NHP moves around the cage.

Other intriguing permutations of the SPAs and mode stirring assemblies can be explored in future research. For example, additional SPAs could be placed on the back wall of the cage (along row A, Fig. 2) in addition to the ceiling to determine whether passive antenna mode stirring could reduce sensitivity to BCI orientation. Future work could also explore whether improved results might be achieved with additional impedance states, e.g. using a single-pole-four-throw switch such as the Analog Devices ADG904 to yield a finer granularity of the phase of reflection at each SPA. Rather than using CMOS RF switch technologies with relatively high insertion loss ($>$1 dB), gallium arsenide (GaAs) RF switches could be explored that have lower two-way insertion loss ($<$1 dB).

Acknowledgment

The authors would like to thank Prof. Azadeh Yazdan-Shahmorad and the team at the Washington National Primate Research Center for providing access to the NHP cage, as well as Apoorva Sharma, Ph.D. for her insightful discussions about the experiments and analysis.

References

[1] C. T. Moritz, S. I. Perlmutter, and E. E. Fetz, "Direct control of paralysed muscles by cortical neurons," *Nature*, vol. 456, pp. 639–642, 2008.

[2] S. Zanos, A. G. Richardson, L. Shupe, F. P. Miles, and E. E. Fetz, "The Neurochip-2: an autonomous head-fixed computer for recording and stimulating in freely behaving monkeys," *IEEE Trans. Neural Syst. Rehabil. Eng.*, vol. 19, no. 4, pp. 427–435, 2011.

[3] M. Yin *et al.*, "Wireless neurosensor for full-spectrum electrophysiology recordings during free behavior," *Neuron*, vol. 84, no. 6, pp. 1170 – 1182, 2014.

[4] A. Jackson, J. Mavoori, and E. E. Fetz, "Correlations between the same motor cortex cells and arm muscles during a trained task, free behavior, and natural sleep in the Macaque monkey," *Physiology*, vol. 97, no. 1, pp. 360–374, Jan. 2007.

[5] D. A. Schwarz, M. A. Lebedev, T. L. Hanson, D. F. Dimitrov, G. Lehew, J. Meloy, S. Rajangam, V. Subramanian, P. J. Ifft, Z. Li *et al.*, "Chronic, wireless recordings of large-scale brain activity in freely moving rhesus monkeys," *Nature Methods*, vol. 11, no. 6, p. 670, 2014.

[6] X. Liu, M. Zhang, A. G. Richardson, T. H. Lucas, and J. V. der Spiegel, "Design of a closed-loop, bidirectional brain machine interface system with energy efficient neural feature extraction and PID control," *IEEE Trans. Biomed. Circuits Syst.*, vol. 11, no. 4, pp. 729–742, Aug 2017.

[7] R. R. Harrison, H. Fotowat, R. Chan, R. J. Kier, R. Olberg, A. Leonardo, and F. Gabbiani, "Wireless Neural/EMG Telemetry Systems for Small Freely Moving Animals," *IEEE Trans. Biomed. Circuits Syst.*, vol. 5, no. 2, pp. 103–111, 2011.

[8] R. Muller, H.-P. Le, W. Li, P. Ledochowitsch, S. Gambini, T. Bjorninen, A. Koralek, J. M. Carmena, M. M. Maharbiz, E. Alon, and J. M. Rabaey, "A minimally invasive 64-channel wireless μECoG implant," *IEEE J. Solid-State Circuits*, vol. 50, no. 1, pp. 344–359, 2015.

[9] J. Rosenthal and M. S. Reynolds, "A 1.0-Mb/s 198-pJ/bit Bluetooth Low-Energy compatible single sideband backscatter uplink for the NeuroDisc braincomputer interface," *IEEE Trans. Microw. Theory Techn.*, vol. 67, no. 10, pp. 4015–4022, Oct. 2019.

[10] J. Rosenthal, A. Sharma, E. Kampianakis, and M. S. Reynolds, "A 25 Mbps, 12.4 pJ/b DQPSK backscatter data uplink for the NeuroDisc braincomputer interface," *IEEE Trans. Biomed. Circuits Syst.*, vol. 13, no. 5, pp. 858–867, Oct. 2019.

[11] Daeyoung Kim, M. A. Ingram, and W. W. Smith, "Measurements of small-scale fading and path loss for long range RF tags," *IEEE Trans. Antennas Propag.*, vol. 51, no. 8, pp. 1740–1749, 2003.

[12] J. D. Griffin and G. D. Durgin, "Complete link budgets for backscatter-radio and RFID systems," *IEEE Ant. Propag. Mag.*, vol. 51, no. 2, pp. 11–25, April 2009.

[13] A. Sharma, E. Kampianakis, J. Rosenthal, A. Pike, A. Dadkhah, and M. S. Reynolds, "Wideband UHF DQPSK backscatter communication in reverberant cavity animal cage environments," *IEEE Trans. Antennas Propag.*, vol. 67, no. 8, pp. 5002–5011, 2019.

[14] J. Rosenthal, A. Pike, and M. S. Reynolds, "A 1 Mbps 158 pJ/bit Bluetooth Low Energy (BLE) compatible backscatter communication uplink for wireless neural recording in an animal cage environment," in *Proc. IEEE Intl. Conf. RFID*, 2019, pp. 1–6.

[15] M. P. Powell, W. R. Britz, J. S. Harper, and D. A. Borton, "An engineered home environment for untethered data telemetry from nonhuman primates," *J. Neuroscience Methods*, vol. 288, pp. 72 – 81, 2017.

[16] M. Ingram, M. Demirkol, and D. Kim, "Transmit diversity and spatial multiplexing for RF links using modulated backscatter," in *Proc. Intl. Symp. Signals, Syst., and Elect.*, 08 2001, pp. 24–27.

[17] J. D. Griffin and G. D. Durgin, "Gains for RF tags using multiple antennas," *IEEE Trans. Antennas Propag.*, vol. 56, no. 2, pp. 563–570, 2008.

[18] M. S. Trotter, C. R. Valenta, G. A. Koo, B. R. Marshall, and G. D. Durgin, "Multi-antenna techniques for enabling passive RFID tags and sensors at microwave frequencies," in *Proc. IEEE Intl. Conf. RFID*, 2012, pp. 1–7.

[19] C. He, S. Chen, H. Luan, X. Chen, and Z. J. Wang, "Monostatic MIMO backscatter communications," *IEEE J. Sel. Areas Commun.*, vol. 38, no. 8, pp. 1896–1909, 2020.

[20] R. Serra, A. C. Marvin, F. Moglie, V. M. Primiani, A. Cozza, L. R. Arnaut, Y. Huang, M. O. Hatfield, M. Klingler, and F. Leferink, "Reverberation chambers a la carte: An overview of the different mode-stirring techniques," *IEEE Electromagn. Compat. Mag.*, vol. 6, no. 1, pp. 63–78, 2017.

[21] G. Andrieu and N. Ticaud, "Performance comparison and critical examination of the most popular stirring techniques in reverberation chambers

using the well-stirred condition method," *IEEE Trans. Electromagn. Compat.*, vol. 62, no. 1, pp. 3–15, 2020.

[22] E. Voges, T. Eisenburger, and D. Peier, "Electrical mode stirring by reactively loaded antennas in reverberating chambers for EMC," in *2007 18th Intl. Zurich Symposium Electromagn. Compat.*, 2007, pp. 465–468.

[23] Y. Liang, R. Long, Q. Zhang, J. Chen, H. V. Cheng, and H. Guo, "Large intelligent surface/antennas (lisa): Making reflective radios smart," *J. Commun. Inf. Netw.*, vol. 4, no. 2, pp. 40–50, 2019.

[24] W. Zhao, G. Wang, S. Atapattu, T. A. Tsiftsis, and X. Ma, "Performance analysis of large intelligent surface aided backscatter communication systems," *IEEE Wireless Commun. Lett.*, vol. 9, no. 7, pp. 962–966, 2020.

[25] G. Vougioukas, A. Bletsas, and J. N. Sahalos, "Instantaneous, zero-feedback fading mitigation with simple backscatter radio tags," *IEEE J. Radio Freq. Identif.*, pp. 1–1, 2020.

[26] O. Yurduseven, S. D. Assimonis, and M. Matthaiou, "Intelligent reflecting surfaces with spatial modulation: An electromagnetic perspective," *IEEE Open J. Commun. Society*, vol. 1, pp. 1256–1266, 2020.

[27] J.-B. Gros, P. del Hougne, and G. Lerosey, "Tuning a regular cavity to wave chaos with metasurface-reconfigurable walls," *Phys. Rev. A*, vol. 101, p. 061801, Jun 2020.

James D. Rosenthal (S'16) received the B.S. degree in electrical engineering from the University of Minnesota, Minneapolis, MN, USA in 2013, and the M.S. degree in electrical engineering from the University of Washington, Seattle, WA, USA in 2018.

From 2013 to 2016 he was an electrical engineer at NASA Langley Research Center, Hampton, VA, USA where he designed avionics systems for aerospace research. Since 2016 he has been a Ph.D. student in the Department of Electrical & Computer Engineering at University of Washington. His research is focused on the design of ultra-low power backscatter communication systems for biomedical applications.

Alexandra Pike received her BA in Physics and French from Grinnell College, Grinnell, IA, USA, in 2008, her M.Litt in Celtic Studies from the University of Aberdeen, Aberdeen, Scotland, in 2010, and her MIT in Secondary Science from the University of Washington, Seattle, WA, USA, in 2012. Since 2012 she has been a Physics teacher at Juanita High School in Kirkland, WA, USA, and in 2017 she became a National Board Certified teacher. During the summers of 2016, 2017, and 2018, she was an NSF Research Experience for Teachers (RET) researcher at UW. Her research interests include high school physics and engineering education and teacher professional development.

Sara Reyes is third-year undergraduate studying electrical engineering at the University of Washington, Seattle, WA, USA. She joined the Sensing, Computing, and Communication Group in spring 2019. Her research interests include ultra-low power backscatter communication systems for biomedical applications, as well as working on functionality and thermal testing for RF tags and antennas for aerospace and military applications.

Matthew S. Reynolds (S'01–M'02–SM'10) received the S.B., M.Eng., and Ph.D. degrees from the Massachusetts Institute of Technology (MIT), Cambridge, MA, USA, in 1998, 1999, and 2003, respectively.

He is currently an Associate Professor of Electrical and Computer Engineering at the University of Washington, Seattle, WA, USA. He is a co-founder of the RFID systems firm, ThingMagic Inc., the demand-side energy conservation technology firm Zensi, the home sensing company SNUPI Inc, and the millimeter wave imaging firm ThruWave Inc. His research interests include the physics of sensors and actuators, RF identification (RFID), microwave and millimeter wave imaging, and sensor signal processing.